

# A TEM study of the combined effect of severe plastic deformation and (Zr), (Sc+Zr)-containing dispersoids on an Al–Mg–Si alloy

M. Cabibbo · E. Evangelista

Received: 22 August 2005 / Accepted: 19 October 2005 / Published online: 6 June 2006  
© Springer Science+Business Media, LLC 2006

**Abstract** The microstructural evolution with strain was investigated in a Zr-modified 6082 Al–Mg–Si alloy and in the same alloy added with 0.117 wt.% Sc, subjected to a multi-pass equal-channel angular pressing, up to a true strain of  $\sim 12$ . The role of fine  $\text{Al}_3(\text{Sc}_{1-x}\text{Zr}_x)$  dispersoids, pertaining Al–Mg–Si–(Sc–Zr) alloy, and  $\text{Al}_3\text{Zr}$  dispersoids, pertaining to Al–Mg–Si–(Zr) alloy, was investigated by transmission electron microscopy techniques and discussed. Compared to the commercial parent alloy, Al–Mg–Si, block wall formation and propagation were favored by the presence of Sc–Zr containing dispersoids, while cell boundary evolution was less affected,  $\text{Al}_3\text{Zr}$  dispersoids affected the microstructure in a similar way, but in a lesser extent. Mean misorientation across block walls increased with strain much more in the Sc–Zr containing alloy, reaching a plateau, starting from a true strain of  $\sim 8$ . Misorientation across cell boundaries continuously increased to  $\sim 8^\circ$  and  $\sim 5^\circ$  for the Sc–Zr and Zr containing alloy, respectively. The effect of the presence of  $\text{Al}_3(\text{Sc}_{1-x}\text{Zr}_x)$  and  $\text{Al}_3\text{Zr}$  in the matrix, on the  $\text{Mg}_2\text{Si}$  particle shearing and Si shrinking phenomena with strain, was also addressed and documented.

## Introduction

There is much current interest in producing metals with very small grain sizes. A reduction in grain size has the

advantage of improving the strength and toughness of the material at room temperature and, if the small grain sizes is retained to elevated temperatures, there is also a potential for achieving good formability and superplastic ductility. However, processing bulk aluminum alloys to sub-micrometer grain sizes is rather difficult, and normally the smallest grain sizes achievable through conventional thermo-mechanical means are  $\sim 15\text{--}20\ \mu\text{m}$  [1–4].

Very fine grained microstructures can only be effectively achieved by using severe deformation methods, such as high-pressure torsion (HPT), reciprocal extrusion, accumulative roll bonding and equal channel angular pressing [1, 5–7]. The latter method, developed almost 20 years ago, by Segal et al. [8], involves subjecting a material to severe plastic deformation by repeatedly shearing a billet under constrained conditions, in a die with two channels of identical cross section meeting at a specific angle and curvature. A wide range of alloys have been deformed using ECAP to grain sizes below  $\sim 1\ \mu\text{m}$ , often resulting in improvements such as increased strength, toughness and fatigue resistance and high strain rate superplasticity [7, 9, 10]. Since the cross-sectional dimensions of the specimen are not modified by passage through the die, repeated pressings may be used to attain very high strains [5, 11].

Recently, two important advances have been made in ECAP processing of metals. First, ECAP has been combined with other metal-working processes to provide a more versatile procedure. In fact, performance of cold rolling after ECAP has been shown to improve the potential for producing an ultrafine grained material in sheet form [12]. Other novel developments include the utilization of a multipass facility or a rotary die in order to achieve high total strains without removing the specimen from the ECAP die [9–14].

M. Cabibbo (✉) · E. Evangelista  
CNR (INFM) / Dipartimento di Meccanica, Università  
Politecnica delle Marche, Via Brecce Bianche, 60131 Ancona,  
Italy  
e-mail: m.cabibbo@univpm.it

Systematic studies on the role of ECAP shear on subgrain and grain evolution have been performed only in recent years. Several investigations [15, 16] have shown that, during deformation, grains in polycrystals subdivide into many small crystallites, each having a crystal orientation rotated toward neighboring and to the original grains. Thus, during straining, dislocations generally arrange into a mosaic-like pattern which is basically composed of dislocations arranged in nearly two-dimensional boundaries surrounding regions which are almost dislocation-free. According to the low-energy dislocation system (LEDS), concept first introduced by Kuhlmann-Wilsdorff [18, 19], during deformation, dislocation structures serve the function of maintaining force equilibrium by strengthening the material to the level of the actual applied stress. Thus, on the basis of this theory, dislocation boundaries are the most thermodynamically possible stable dislocation arrangement. Furthermore, even for the same wall crystallographic orientation, the energy per unit length of dislocation can be reduced by increasing the boundary rotation angle (i.e., its misorientation) [19]. Parameters such as dislocation density and dislocation boundary spacing (pertaining to both cells and grains) are generally used for flow stress and microstructural refining mechanism determination. Under severe plastic deformation (SPD), dislocation boundaries evolve into a regular pattern of grain subdivisions, belonging to two scales: large-scale long, continuous high-angle dislocation boundaries (HABs), i.e., block walls, and small-scale incidental low-angle dislocation boundaries (LABs), i.e., cells [20–27]. In a commercial aluminum alloy, the boundary spacing and misorientation angle distribution of HABs and LABs evolve differently as a function of strain; in particular, they exhibit different morphologies at small to medium strains, but similar at high strains [20, 21, 24, 25].

The high age-hardenability of Al–Mg–Si alloys is due to the considerable secondary phase particles precipitation during heat treatments. The importance of the age-hardening response in the 6XXX family of aluminum alloys, such as 6082, has promoted several investigations into their precipitation process kinetics leading to the identified of  $\beta$ -Mg<sub>2</sub>Si and Si rounded, almost spherical, particles as the predominant secondary phase precipitates and of some other quaternary precipitates. The following precipitation sequence takes place for the Mg<sub>2</sub>Si phase: (i) Aluminum supersaturated solid solution (SSS); (ii) clustering of Si and Mg atoms; (iii) dissolution of Mg clusters and formation of Mg/Si co-clusters (GP-I zone); (iv)  $\beta''$  needles (GP-II zone); (v)  $\beta'$  rod precipitates; (vi)  $\beta$  (Mg<sub>2</sub>Si) stable plates [29–34]. In the last decades, the need for improving the mechanical properties of light alloys has oriented industry's attention and the research efforts toward two different, but parallel, fields. One concerns the process of age-hardening of such

alloys and tended to improve the strength by introducing new alloying elements, such as RE, Zr, Sc, Ag; the other tackled the development of new metal processing techniques to refine the microstructure and thus improve the mechanical strength [35–37].

The requirement of a small and stable grain size is usually achieved by using either two-phase alloys or materials containing precipitates that impede grain boundary mobility and thereby restrict grain growth. The latter is a specific peculiarity of Sc–Zr containing dispersoids which are able to effectively pin low and high angle boundaries together with free dislocations [37]. Aluminum alloyed with scandium, or zirconium, has excellent mechanical properties at room temperature, due to the presence of coherent, nanometer size Al<sub>3</sub>Sc(Zr) precipitates effectively dispersed either in the grain boundaries and within grains, thus blocking mobile dislocations and stabilizing a fine-grained structure [37, 38]. These Al<sub>3</sub>Sc(Zr) precipitates are more stable than coarsening 6xxx series alloys, whose microstructures coarsen upon reheating of the material. Scandium-containing aluminum alloys thus constitute castable, heat-treatable, precipitation-strengthened alloys that can be used at temperatures significantly higher than conventional aluminum alloys. Combined additions of Sc and Zr were shown to be more effective in refining as-cast material microstructures. Zr is able to replace some of the Sc in Al<sub>3</sub>Sc, giving rise to Al<sub>3</sub>(Sc<sub>1-x</sub>Zr<sub>x</sub>) dispersoids having an L12 crystal structure like the Al<sub>3</sub>Sc [36–40]. Loss in coherency of either Al<sub>3</sub>Zr and Al<sub>3</sub>(Sc<sub>1-x</sub>Zr<sub>x</sub>) dispersoids has been documented to promote an increase in particle coarsening rate and in their spacing. This effect produces a decrease in the dispersoids pinning efficiency against boundary migration and dislocation pinning [40–42]. According to [40], the typical radius for coherent-to-semicoherent dispersoids transition is in the range 15–40 nm, the size-activated particles coarsening being actually delayed in that dimensional range, which corresponds to a coherent and semicoherent dispersoids coexistence condition.

The present paper aims at presenting some experimental results on the role of Zr and Sc–Zr containing dispersoids in two 6082 Al–Mg–Si alloys in the T8 condition, and then subjected to severe plastic deformation and discussing the formation and evolution of block walls and cells with strain in both alloys.

## Experimental procedures and method

The material was supplied by Hydro-Norsk (Trondheim, Norway) in the form of extruded cylindrical billets 10 mm in diameter. The chemical composition of the two alloys is reported in Table 1 (wt.%). According to Table 1, the

**Table 1** Chemical composition (wt.%) of Al–Mg–Si–(Zr), alloy 1, and Al–Mg–Si–(Sc–Zr), alloy 2

| (wt.%)  | Mg   | Si   | Fe   | Mn    | Zr   | Sc    |
|---------|------|------|------|-------|------|-------|
| Alloy 1 | 0.34 | 0.51 | 0.16 | 0.014 | 0.10 | –     |
| Alloy 2 | 0.33 | 0.52 | 0.17 | 0.014 | 0.10 | 0.117 |

Al–Mg–Si–(Zr) alloy will be designated as alloy 1, and Al–Mg–Si–(Sc–Zr) as alloy 2. The microstructural study was carried out on the material subjected to T8 (solution treatment at 803 K/4 h, quenching and overaging at 463 K/8 h), followed by ECAP to a true strain of  $\sim 12$ . T8 treatment was carried out to completely homogenize the alloy microstructure, avoiding the possibility of secondary phase precipitation during following deformation. The heat treatment is expected to have allowed the complete precipitation of the secondary phases leaving a minimum solid solution level in the matrix of the material being deformed. Thus, the study of the role of  $\text{Al}_3\text{Zr}$  and  $\text{Al}_3(\text{Sc}_{1-x}\text{Zr}_x)$  dispersoids on the boundary generation and evolution and their influence on the high density dislocation interaction with the secondary phase particles, was facilitated. Eventually, the heat treated specimens were subjected to ECAP at room temperature using the so-called “route B<sub>C</sub>” [9] (a + 90° billet rotation at each pass) for a maximum of 12 passes. This route was selected because experiments on pure aluminum have shown that it leads most effectively to a homogeneous microstructure of essentially equiaxed grains separated by high-angle grain boundaries [28]. The ECAP die configuration was designed so as to have two intersecting channels meeting at an angle of 90° and an outer arc of curvature of 45°, inducing an equivalent strain of approximately 1 after each pass through the die (i.e., a strain of 1.05 at each pass) and thus generating a maximum strain of  $\sim 12$ , after the twelfth pass [8, 10, 13, 14]. The ECAP die was made of a block of SK3 tool steel (Fe-1.1%C), according to the design reported in [43]. Billets for microstructural inspections were sectioned along the Y-plane [9, 14] (essentially along the extruding direction), containing the pressing direction (PD) and the transverse direction.

Polarized optical microscopy (POM) images were acquired from specimen surfaces etched by using a solution of  $\text{HBF}_4$  in ethanol at 273 K and 12 V. Thin foils were mechanically prepared to a thickness of  $\sim 120$   $\mu\text{m}$ , then 3-mm discs were punched and electro-polished using a solution of 1/3  $\text{HNO}_3$  and methanol at 240 K and 18 V. A Philips<sup>TM</sup> CM200 transmission electron microscope, operating at 200 kV, equipped with double tilt specimen holder, was used. To optimize particles inspection, transmission electron microscopy (TEM) studies were carried out by titling discs so that their surface lay near the [001] zone axis, revealing the  $\langle 100 \rangle$  edge of squared-shape  $\text{Al}_3\text{Zr}$

and  $\text{Al}_3(\text{Sc}_{1-x}\text{Zr}_x)$  dispersoids.  $\text{Al}_3(\text{Sc}_{1-x}\text{Zr}_x)$  and  $\text{Al}_3\text{Zr}$  dispersoids was detected by dark-field imaging utilizing the (100) and (110) diffraction spots of the precipitates. Identification of other phases ( $\text{Mg}_2\text{Si}$ , Si and Fe-rich quaternary intermetallic  $\text{Al}_{15}(\text{Fe},\text{Mn})_3\text{Si}_2$ ) was performed by using a combination of energy dispersive X-ray spectroscopy (EDS) and selected area electron diffraction patterns (SAEDPs). Precipitate density is calculated from the number of precipitates per area unit divided by the thickness of the foil. Local thickness was calculated by computer assisted in situ direct measurements. Mean number and size of secondary phase particles were calculated using a computer assisted image analysis facility. Boundary misorientation was quantitatively characterized in the TEM by using Kikuchi pattern analysis, and Moiré fringes for those boundaries showing it (typically less than  $\sim 5^\circ$  in misorientation) [26]. For each TEM disc (i.e., each experimental condition), the relative misorientation of typically 50 boundaries was measured.  $\text{Al}_3\text{Zr}$  and  $\text{Al}_3(\text{Sc}_{1-x}\text{Zr}_x)$  dispersoid density was determined by dark-field TEM inspections on at least 20 different zones, at a magnification of 50 kX, and by using the linear intercept method. Thin disc local thickness was measured by the extinction contour method.

Micro-hardness tests were carried out by applying a load of 100 g for 15 s, and average data were calculated from a series of 20 independent measurements repeated for each condition.

## Results and discussion

Figure 1(a), (b) shows the microstructure of alloy 1 and 2, respectively in the as-extruded, purchased state. Very elongated grains characterize the microstructure of either alloys with a narrower lateral spacing in the case of the alloy containing Sc (alloy 2), compared to the case of alloy 1, grain lateral spacing being of  $\sim 45$   $\mu\text{m}$  and  $\sim 38$   $\mu\text{m}$ , for alloy 1 and 2, respectively. The inset, in Fig. 1(a) and (b) shows a sectional view of the microstructure from which the estimation of the lateral grain spacing (appearing elongate along the longitudinal section, i.e., the extruded direction) is greatly favored.

Figure 2(a), (b) shows two POM images of the extruded and T8 treated materials along the Y-plane, for alloy 1 and 2, respectively. The very elongated grains of the extruded

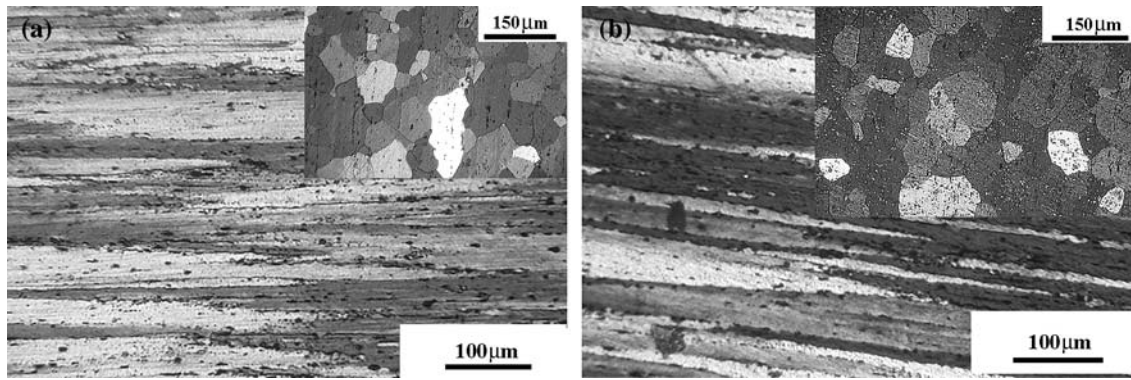


**Fig. 1** POM images of the as-extruded microstructure of Al–Mg–Si–(Zr), alloy 1 (a), and Al–Mg–Si–(Sc–Zr), alloy 2 (b). The inlet shows the sectional plane microstructure

T8 treated alloy 2 appeared thinner than the alloy 1 in the same condition. This is primarily due to more diffuse and larger number of fine  $\text{Al}_3(\text{Sc}_{1-x}, \text{Zr}_x)$  fine dispersoids, which appear more effective in pinning boundaries than in the material with  $\text{Al}_3\text{Zr}$  dispersoids. It is interesting to note that the T8 heat treatment generated a recrystallized microstructure still exhibiting fairly elongated grains in both cases. As a matter of fact, recrystallization was much more effectively retarded by the  $\text{Al}_3(\text{Sc}_{1-x}, \text{Zr}_x)$  dispersoids (alloy 2), compared with the far less densely dispersed  $\text{Al}_3\text{Zr}$  dispersoids, which characterize the alloy 1 microstructure. Average dispersoids density has been calculated to be as high as  $1.5 \times 10^{20} \text{ m}^{-3}$  and  $4.8 \times 10^{19} \text{ m}^{-3}$  for  $\text{Al}_3(\text{Sc}_{1-x}, \text{Zr}_x)$  and  $\text{Al}_3\text{Zr}$  dispersoids, respectively. This means that the density of Sc-containing dispersoids are more than three times as high as  $\text{Al}_3\text{Zr}$ . This is due to either a higher (Sc + Zr) concentration in alloy 2, respect to Zr in alloy 1, and to slightly coarser dimensions of  $\text{Al}_3\text{Zr}$ , being of 38 nm in average, compared to 25 nm of the  $\text{Al}_3(\text{Sc}_{1-x}, \text{Zr}_x)$ . These data indicate the Sc addition to markedly favor the dispersoids precipitation finely disperse in the whole material's microstructure. A significant consequence of this higher Sc-dispersoids fraction is surely responsible for a different lateral grain spacing for the two alloys. In fact, the mean transverse grain spacing of the alloy 1 and 2 is of  $\sim 20 \mu\text{m}$  and  $\sim 12 \mu\text{m}$ , respectively, which means that the presence of the complex  $\text{Al}_3(\text{Sc}_{1-x}, \text{Zr}_x)$  dispersoids considerably reduces the post-T8 grained microstructure (Fig. 2(a), (b)). Moreover, recrystallisation induced by the T8 treatment in presence of dispersoids greatly contributed to reduce the grained structure more than halving the lateral grain spacing. Vetrano et al. [44], in their study, suggested that  $\text{Al}_3\text{Sc}$  dispersoids have a coherency level higher than the  $\text{Al}_3(\text{Sc}_{1-x}, \text{Zr}_x)$ . This result in a more effective pinning phenomena of HABs of the formed, compared to the latter. This is believed to be due to the presence of Zr within the chemical structure of  $\text{Al}_3(\text{Sc}_{1-x}, \text{Zr}_x)$ , which, for his more than double density compared to Sc, and its

bigger radius, contributes to limit the dispersoid size range of coherency.

The macroscopic effect of the shear bands after the first pass is illustrated in Fig. 2(c), (d), which are two polarized optical images. The microstructure at the maximum strain of  $\sim 12$  of both materials is illustrated in Fig. 2(e), (f), which reports two representative low-magnification TEM images of alloy 1 and 2, respectively. The major difference consists of a remarkable presence of very narrow strips ( $< 1 \mu\text{m}$ ) of high-angle boundaries interrupted by intersecting high and low angle boundaries, which contribute to form fine grains and cells. The microstructure of alloy 1 shows a considerable fraction of equiaxed sub-micrometer grains and cells, together with elongated HABs. Microstructure differences between the two alloys, consisted in the a scale factor in the boundary evolution with strain, that is, the HABs spacing and fine equiaxed structures (either grains and cells) were constantly wider in the alloy 1, compared to same strain microstructure of alloy 2. This is clearly due to the diffuse presence of the fine  $\text{Al}_3(\text{Sc}_{1-x}, \text{Zr}_x)$  dispersoids, that have a mean equivalent diameter of 25 nm and a mean spacing on the (100) plane of 560 nm, compared to the 38 nm average size of  $\text{Al}_3\text{Zr}$ , with a spacing of 1,020 nm. Micro-hardness and electrical conductivity (Fig. 3) show continuously increasing and decreasing trends with strain, respectively. Hardness consistently increases with strain in both alloy 1 and 2, alloy 1 being constantly less hard by 10–15%. This difference in hardness could be attributed to a less effective microstructure refinement, in the alloy containing the  $\text{Al}_3\text{Zr}$ , that retard the formation of fine HAB structures. The quick and effective microstructure refinement is prevalently responsible for the increased hardness values with strain, while addition of Sc to alloy 1, contributed to further hardening of the material, over the whole range of strain. At the same time, the electrical conductivity steadily decreases with strain, the material not containing Sc having consistently higher values respect the one with Sc. This is clearly due to the

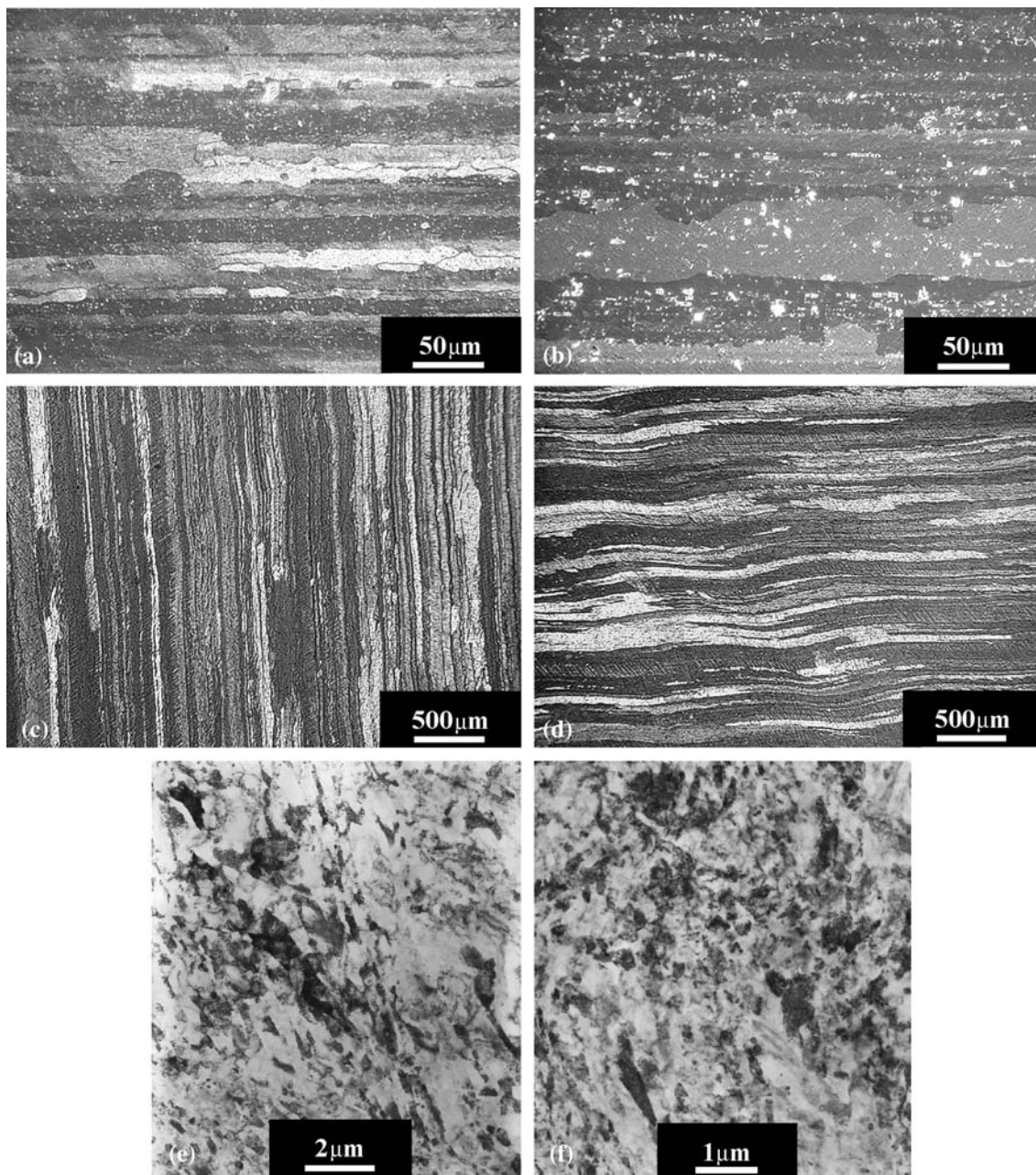


**Fig. 2** Microstructure of alloy 1, (a), (c), (e) and alloy 2, (b), (d), (f). (a), (b) are polarized optical images of the as-extruded and T8 condition; (c), (d) are polarized optical images of the microstructure

after the first pass and showing the shear bands; (e), (f) are low-magnification TEM images of the materials subjected to 12 passes

diffuse presence, within the grains, of the nanometer  $\text{Al}_3(\text{Sc}_{1-x}\text{Zr}_x)$  dispersoids, capable of continuously pinning dislocations and cell boundaries resulting in a larger reduction in conductivity in a much more effective way than in  $\text{Al}_3\text{Zr}$ . An important point is which factors are responsible for the higher strength:

1. higher dispersoid density
2. greater dispersoid coherency
3. more refined grain size due to differences in the pinning abilities of the two different dispersoids

4. differences in the dislocation density due to relatively different stabilization abilities of the two different dispersoids

4. differences in the dislocation density due to relatively different stabilization abilities of the two different dispersoids

POM inspections showed coarse scale deformation banding within some grains, although other grains appeared to have deformed more homogeneously. More detailed microstructural examination revealed well-defined cellular structures bounded by diffuse arrays of dislocations. Figure 4(a)–(d) shows some representative TEM

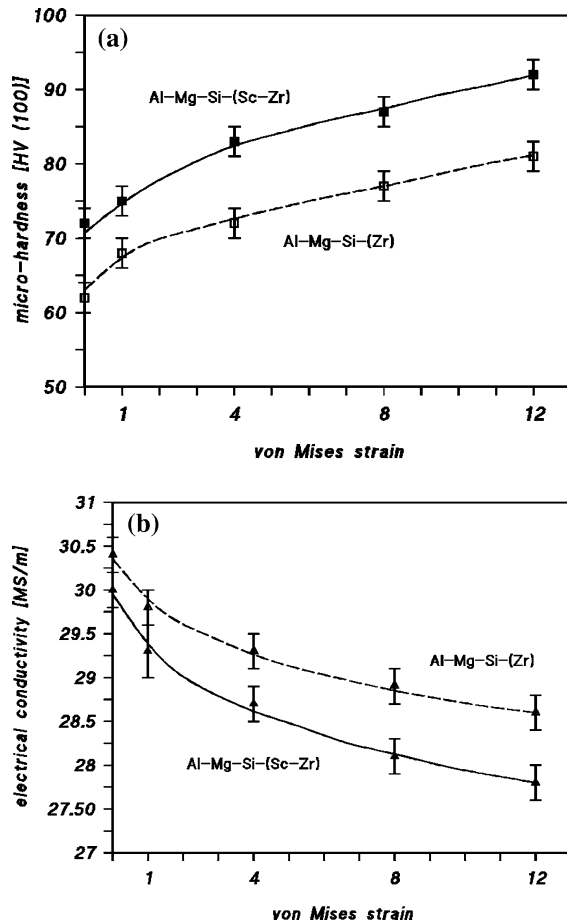


**Fig. 3** Micro-hardness (a) and electrical conductivity (b) as a function of true strain. The two plots refer to both alloys, with and without Sc

images of both materials after 1 and 12 passes. The cells, which were found to contain high levels of interior dislocations, had a mean size of  $\sim 2 \mu\text{m}$  after the first pass in presence of Sc, and of  $\sim 5 \mu\text{m}$  in the other material; cell boundary misorientation was mainly of  $4\text{--}5^\circ$ , and  $1\text{--}2^\circ$ , respectively. Cell size shrank with strain more effectively in alloy 2, reaching a mean size of  $\sim 330 \text{ nm}$ , after 8 passes, and  $\sim 250 \text{ nm}$  after a strain of 12, while it was considerably less pronounced in the material not containing Sc, reaching the value of  $\sim 720 \text{ nm}$ , after 8 passes, and  $\sim 450 \text{ nm}$  at a strain of 12. The cell boundary misorientation increased much more in the presence of the  $\text{Al}_3(\text{Sc}_{1-x}, \text{Zr}_x)$  dispersoids to a mean value of  $\sim 8^\circ$ , compared with  $\sim 5^\circ$  in alloy 1. In alloy 1, the  $\text{Al}_3\text{Zr}$  dispersoids are mostly coherent and spherical, which are heterogeneous distributed throughout the matrix; in alloy 2, the Sc-containing dispersoids are much more homogeneously distributed. In Fig. 5(a) the mean misorientation of cell and grain boundaries (essentially block walls) is plotted as a function of the strain. The effect of  $\text{Al}_3(\text{Sc}_{1-x}, \text{Zr}_x)$  is apparent in the higher increasing rate of misorientation of both block walls and cell

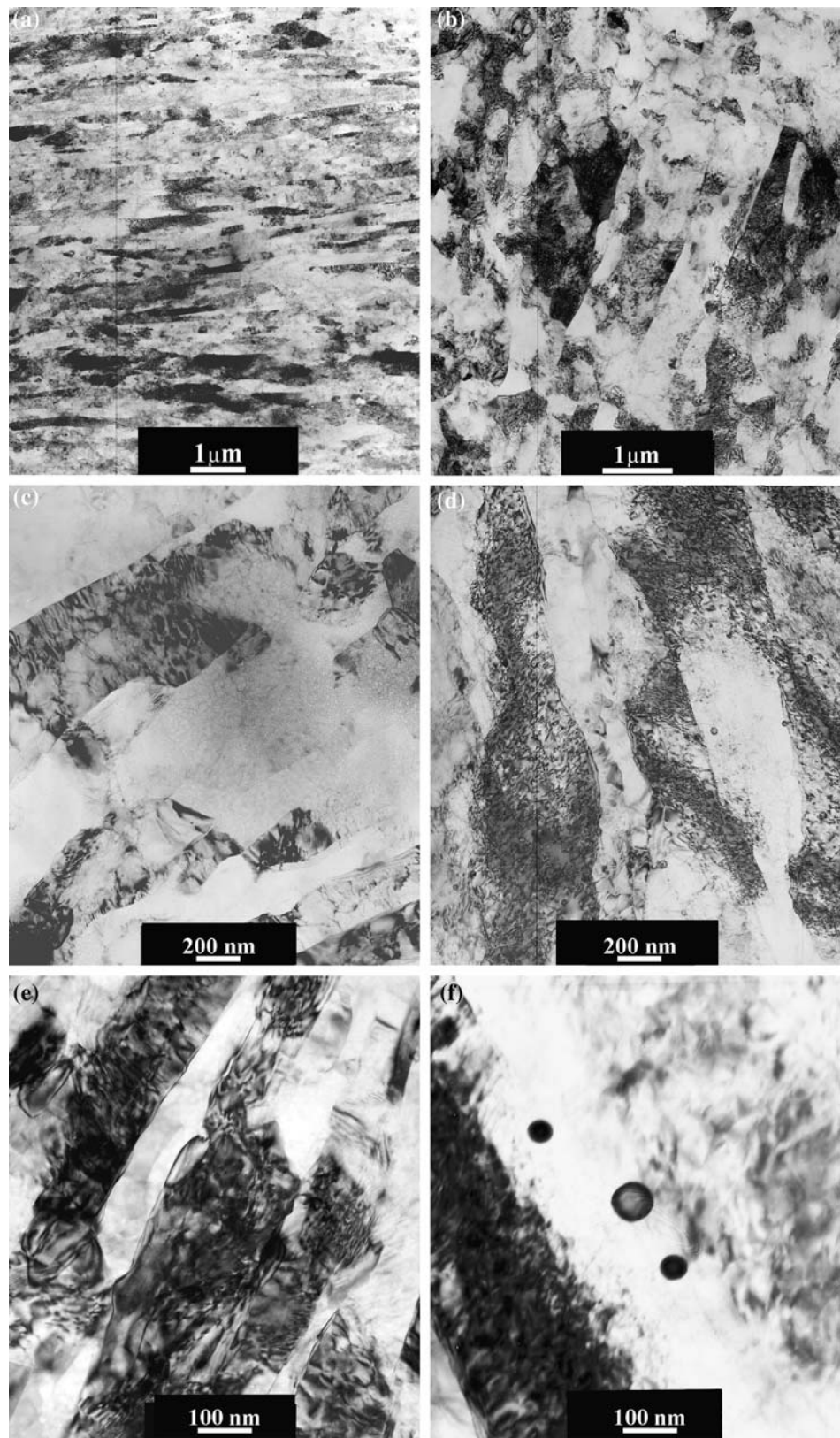
boundaries, which increase to a greater extent than in the alloy with  $\text{Al}_3\text{Zr}$  dispersoids. The deformation and microstructure refining mechanism is believed to be greatly influenced by the spatial distribution and size of the fine dispersoids. In a sense, they act as preferential deforming paths for the deformation bands, which control the refining process.

Dispersoids pin not only free dislocations and tangling dislocations, but, if possible, even more effectively, also cell boundaries and the newly introduced deformation bands. Both block walls and cell boundaries, generated during deformation, are made to flow and slide within the microstructure by the effect of the specific die geometry, shearing the original microstructure at an angle of  $\sim 45^\circ$  with respect to the pressing direction, as is the case of aluminum alloys not containing dispersoids [7, 9–14, 17, 35]. As a matter of fact, boundaries evolution is sensitive to the fine dispersoids spatial distribution. More specifically, in the present study, both alloys showed a non-uniform dispersoids distribution, in that they are primarily located along rows almost parallel to the extrusion direction of the bars. Thus, dispersoids lying along the formed extruded direction, pin the newly formed boundaries. The combination of the strong boundary pin capability and their preferred spatial distribution is able to generate a quick misorientation increment, at each strain leap, especially on the previously generated boundaries. As a consequence, the larger fraction of HABs and LABs, with respect to the material containing  $\text{Al}_3\text{Zr}$  dispersoids, is generated by the continuous misorientation increment driven by the  $\text{Al}_3(\text{Sc}_{1-x}, \text{Zr}_x)$  dispersoids (Fig. 5(b)). (Fig. 6)

In a previous manuscript [35], M. Cabibbo and co-workers documented and reported a breaking-up of  $\text{Mg}_2\text{Si}$  and shrinking of Si particles in a similar 6082-T8 Al–Mg–Si alloy subjected to ECAP. The same investigations were carried out for the alloy 1 and 2 and results are reported in Table 2, where for convenience, the data, published in [35], and related to the parent Al–Mg–Si T8 alloy, are also reported. Figure 7 shows a representative Bright-field TEM image documenting the  $\text{Mg}_2\text{Si}$  breaking up and Si shrinking phenomenon induced by the increasing severe plastic deformation. This process was actually visible in different regions of the specimen and was rather diffuse, irrespective of the vicinity of a cell or grain boundary.

Figure 7(a), (b) shows a plot of the  $\text{Mg}_2\text{Si}$  and Si fraction  $f$  ( $f = 4\pi d_{\text{eq}}^3 N_V/3$ ) and spacing ( $\lambda$ ), respectively, as a function of strain of alloy 1 and 2; the data related to the base material (Al–Mg–Si T8 alloy) and published in [35] are also reported for comparison. The major aspect is by far the remarkable  $\text{Mg}_2\text{Si}$  size reduction with strain (especially after the first pass), whilst Si particles reduction effect is rather limited. These considerations hold much more in the case of alloy 1 than alloy 2, revealing a Sc-containing

**Fig. 4** TEM images of Al–Mg–Si–(Zr) and treated Al–Mg–Si–(Sc–Zr), after 1 pass: (a) and (b), after 4 passes: (c) and (d), and after 12 passes (e) and (f), respectively



dispersoids effect on the microstructural deforming aspects occurring through the increasing severe plastic deformation.

The very interesting aspect in the present case is the reduced scale of the former phenomenon following severe plastic deformation, especially in the material containing

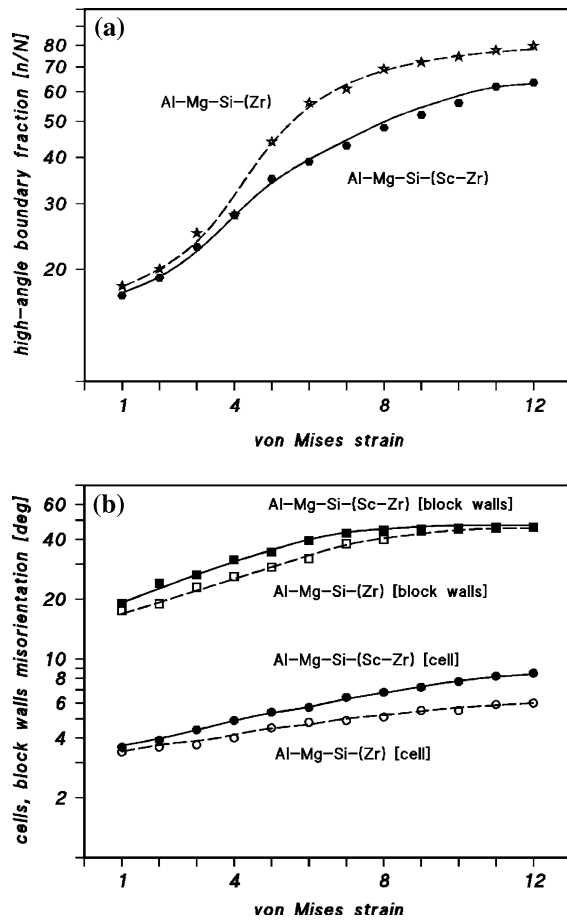
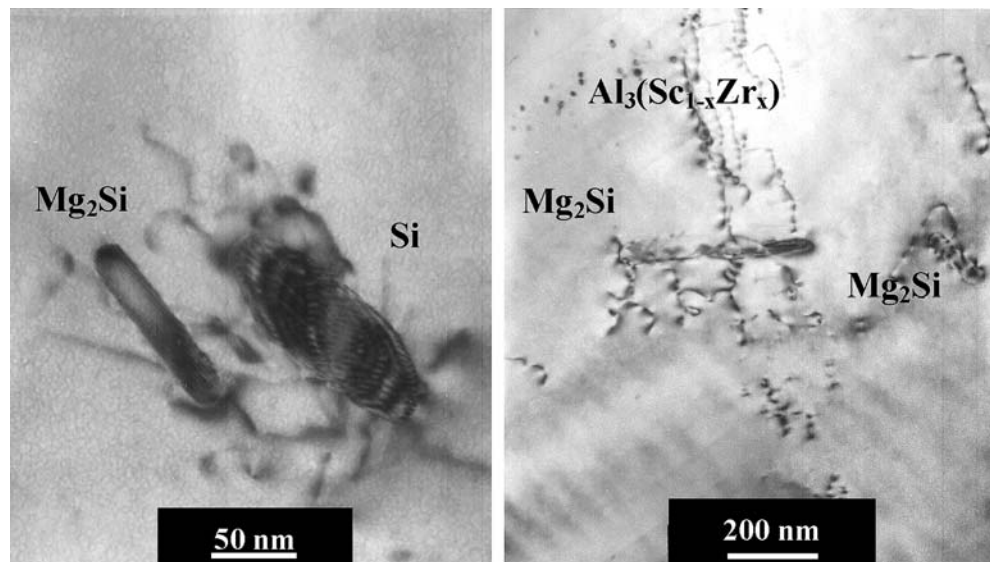


**Fig. 5** Comparison of both materials on high angle boundary fraction (a), and on mean cell and block wall misorientation (b) as a function of strain

$\text{Al}_3(\text{Sc}_{1-x}\text{Zr}_x)$  dispersoids, compared to the case presented in [35]. In fact, in [35], a strong influence of the high dislocation density introduced into the microstructure

**Fig. 6** BF-TEM showing the severe plastic deformation induced  $\text{Mg}_2\text{Si}$  breaking up and Si shrinking phenomenon



during ECAP, on the secondary phase particles distribution (i.e., size and spacing) was documented and discussed. A redistribution in the matrix, of Mg and Si atoms previously forming the long, needle-like  $\text{Mg}_2\text{Si}$  particles which were cut off by the glide dislocations was documented by either TEM and DSC analyses. It was also pointed out that the first ECAP pass is mainly responsible for bulk of the  $\text{Mg}_2\text{Si}$  particles fragmentation and for the partial dissolution of Si particles, as also reported in Table 1, in the present work. Thus, the  $\text{Mg}_2\text{Si}$  fine particles produced contributed more effectively to the dislocation hardening by pinning them and thus further enhancing the formation of dislocation cell networks within the deformed grains. The partial dissolution of Si particles might be due to their spherical morphology favouring, to some extent, a local lattice re-distribution of Si due to the effect of the very high dislocation density produced by the severe plastic deformation.

Dispersoids are believed to be able to inhibit the effect of dislocations in cutting and partially dissolving  $\text{Mg}_2\text{Si}$  and Si particles, respectively, by effectively pinning them while leaving a small fraction of them free to act on the secondary phase particles. The rather low density of fine particles of Si and  $\text{Mg}_2\text{Si}$  secondary phase, is basically due to the overaging treatment at 463 K/8 h, which induced a bulky particle growing to a micrometer scale. These were not taken into account in the Orowan strengthening calculations as a function of strain due to their far less effectiveness in alloy hardening (Table 2).

## Conclusions

The microstructure of a 0.10wt.%Zr-modified 6082-T8 alloy with and without 0.117wt.%Sc addition has been

**Table 2** Mean equivalent diameter ( $d_{eq}$ :  $S = \pi d_{eq}^2/4$ ), number per volume unit ( $N_V$ ) and centre-to-centre spacing ( $\lambda$ ) of  $Mg_2Si$  and Si secondary phase particles in alloy 1 and 2, as a function of strain

| Alloy 1* Al–Mg–Si–(Zr)    | **       | $d_{eq}$ [nm] | $N_V$ [ $10^{19}/m^3$ ] | $\lambda$ [nm] |
|---------------------------|----------|---------------|-------------------------|----------------|
| As-extruded + T8          | Si       | 130           | 1.05                    | 1,090          |
|                           | $Mg_2Si$ | 185           | 1.30                    | 810            |
| ECAP 1 pass               | Si       | 118           | 0.90                    | 1,420          |
|                           | $Mg_2Si$ | 168           | 0.85                    | 1,160          |
| ECAP 8 passes             | Si       | 116           | 0.60                    | 1,530          |
|                           | $Mg_2Si$ | 125           | 0.80                    | 1,220          |
| ECAP 12 passes            | Si       | 102           | 0.45                    | 1,810          |
|                           | $Mg_2Si$ | 115           | 0.50                    | 1,620          |
| Alloy 2* Al–Mg–Si–(Zr–Sc) | **       | $d_{eq}$ [nm] | $N_V$ [ $10^{19}/m^3$ ] | $\lambda$ [nm] |
| As-extruded + T8          | Si       | 145           | 1.00                    | 1,050          |
|                           | $Mg_2Si$ | 190           | 1.35                    | 780            |
| ECAP 1 pass               | Si       | 130           | 0.90                    | 1,140          |
|                           | $Mg_2Si$ | 200           | 0.95                    | 900            |
| ECAP 8 passes             | Si       | 120           | 0.80                    | 1,250          |
|                           | $Mg_2Si$ | 165           | 1.20                    | 905            |
| ECAP 12 passes            | Si       | 125           | 0.95                    | 1,160          |
|                           | $Mg_2Si$ | 160           | 1.05                    | 980            |
| Al–Mg–Si* (AA6082) [35]   | **       | $d_{eq}$ [nm] | $N_V$ [ $10^{19}/m^3$ ] | $\lambda$ [nm] |
| T8                        | Si       | 100           | 1.15                    | 490            |
|                           | $Mg_2Si$ | 160           | 3.30                    | 1,390          |
| ECAP 1 pass               | Si       | 120           | 0.65                    | 4,570          |
|                           | $Mg_2Si$ | 150           | 0.75                    | 3,030          |
| ECAP 4 passes             | Si       | 110           | 0.65                    | 4,540          |
|                           | $Mg_2Si$ | 135           | 1.15                    | 2,640          |
| ECAP 6 passes             | Si       | 100           | 0.60                    | 4,560          |
|                           | $Mg_2Si$ | 110           | 1.40                    | 2,660          |

\*Only the nanometre-scale particles are here considered

\*\*Associated error: 5%

investigated by means of transmission electron microscopy techniques, as a function of the increasing severe plastic deformation throughout ECAP.

The major results can be highlighted as follows:

- (i) The very elongated grains of the extruded (Sc–Zr)-containing and T8 treated material were thinner than ones of the Zr-containing material, the mean transverse grain spacing being  $\sim 12 \mu m$  and  $\sim 20 \mu m$ , respectively.  $Al_3(Sc_{1-x},Zr_x)$  dispersoids were finer and more densely distributed throughout the matrix, compared to the  $Al_3Zr$ .
- (ii) The presence of the very fine  $Al_3(Sc_{1-x},Zr_x)$  dispersoids, in the (Al–Mg–Si)–Zr alloy has highlighted some complex and important effects. The dispersoids effectively reduce the block walls spacing and cell size. HAB evolution with strain was inhibited by the presence of dispersoids. More specifically,  $Al_3(Sc_{1-x},Zr_x)$  were highly coherent with the matrix, finer and more diffuse, than  $Al_3Zr$ , resulting in a further retardation of formation of HABs. This because, dispersoids effectively pinned tangled dislocations

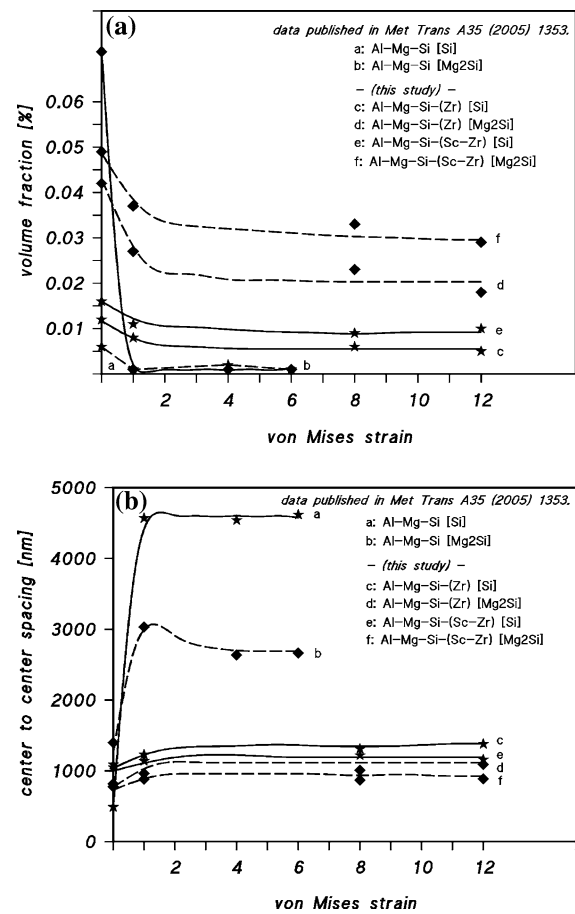


**Fig. 7** Plot of the  $Mg_2Si$  and Si particles fraction  $f$  ( $f = \pi d_{eq}^3 N_V/6$ ) (a), and spacing  $\lambda$  (b) versus strain of both alloy 1 and 2; the data related to the base Al–Mg–Si T8 alloy, and published in [35], are also reported

generating a large fraction of free dislocations, strongly inhibiting the generation of LAB cells. Especially for the early stages of deformation (i.e., first passes), the vast majority of the newly formed boundaries were block walls (both LAB and HAB) directly formed by the shear deformation. At the same time, the misorientation of the formed boundaries kept increasing quickly, and again, faster in the alloy with  $Al_3(Sc_{1-x},Zr_x)$ .

- (iii) A very interesting aspect is the reduced phenomenon of breaking-up of  $Mg_2Si$  particles and Si shrinkage, generated by the effect of the severe plastic deformation, especially in the material containing  $Al_3(Sc_{1-x},Zr_x)$  dispersoids, compared with the parent Al–Mg–Si (6082) T8 alloy.

TEM inspections allowed to calculate the specific contribution to the Orowan strengthening of  $Mg_2Si$  and Si. During the severe plastic deformation,  $\beta$ - $Mg_2Si$  particles showed a widespread tendency to fragment, and the finer

particles were more effective in pinning the dislocations. By contrast, Si tended to dissolve under SPD and its strengthening effect was drastically reduced.

**Acknowledgements** The results presented in this work are part of a research project financially supported by the Italian Ministry of Research (MIUR). The authors wish to acknowledge Mr. D. Ciccarilli for his help in preparing specimen surfaces for the POM inspections.

## References

- Furukawa M, Horita Z, Nemoto M, Langdon TG (2002) *Mater Sci Eng A* 324:82
- Gleiter H (1981) In: Hansen N, Horsewell A, Leffers T, Lillholt H (ed) *Deformation of polycrystals: mechanisms and microstructures*, Risø National Laboratory, Roskilde, Denmark, p 15
- Sanders PG, Fougere GE, Thompson LJ, Eastman JA, Weertman JR (1997) *Nanostruct Mater* 8:243
- Eckert J, Holzer JC, Krill CE, Johnson WL (1992) *J Mater Res* 7:1751
- Koch CC (1997) *Nanostruct Mater* 9:13
- Gholinia A, Humphreys FJ, Prangnell PB (2002) *Acta Mater* 50:4461
- Horita Z, Fujinami T, Langdon TG (2001) *Mater Sci Eng A* 318:34
- Segal VM, Reznikov VI, Drobyshvskiy AE, Kopylov VI (1981) *Russ Metall* 1:99
- Furukawa M, Horita Z, Langdon TG (2002) *Mater Sci Eng A* 332:97
- Akamatsu H, Fujinami T, Horita Z, Langdon TG (2001) *Scripta Mater* 44:759
- Nishida Y, Arima H, Kim J-C, Ando T (2000) *J Japan Inst Light Metals* 50:655
- Stolyarov VV, Zhu YT, Raab GI, Zharikov AI, Valiev RZ (2004) *Mater Sci Eng A* 385:309
- Komura S, Furukawa M, Horita Z, Nemoto M, Langdon TG (2001) *Mater Sci Eng A* 297:111
- Iwahashi Y, Horita Z, Nemoto M, Langdon TG (1997) *Acta Mater* 45:4733
- Zhu YT, Lowe TC (2000) *Mater Sci Eng A* 291:46
- Kamachi M, Furukawa M, Horita Z, Langdon TG (2003) *Mater Sci Eng A* 347:223
- Cabibbo M, Evangelista E, Scalabroni C. (2005) *Micron* 36:401
- Kuhlmann-Wilsdorf D (1989) *Mater Sci Eng A* 113:1
- Kuhlmann-Wilsdorf D (1999) *Acta Mater* 47:1697
- Apps PJ, Bowen JR, Prangnell PB (2003) *Acta Mater* 51:2811
- Liu Q, Juul Jensen D, Hansen N (1998) *Acta Mater* 46:5819
- Shan A, Moon IG, Park JW (2002) *J Mater Proc Technol* 122:255
- Skalli A, Fortunier R, Fillit R, Driver JH (1985) *Acta Metall* 33:997
- Godfrey A, Hughes DA (2002) *Mater Charact* 48:89
- Hansen N, Juul Jensen D (1992) *Acta Metall* 40:3265
- Cabibbo M, Evangelista E (2004) *Proc. of ICAA-9*, ed. IMEA, Brisbane, Australia, p 190
- Cabibbo M, Evangelista E, Latini V (2004) *J Mater Sci* 39:5659
- Sun PL, Kao PW, Chang CP (2004) *Metall Mater Trans A* 35:1359
- Gupta AK, Lloyd DJ, Court SA (2001) *Mater Sci Eng A* 316:11
- Edwards GA, Stiller K, Dunlop GL, Couper MJ (1998) *Acta Mater* 46:3893
- Maruyama N, Uemori R, Hashimoto N, Saga M, Kikuchi M (1997) *Scripta Mater* 36:89
- Li S, Zhao S, Pan M, Zhao D, Chen X, Barabash OM, Barabash RI (1997) *Mater Trans JIM* 38:553
- Matsuda K, Gamada H, Fuji K, Uteni Y, Sato T, Kamis A, Ikeno S (1998) *Metall Mater Trans A* 29:1161
- Van Rooyen M, Sinte Maartensdijk JA, Mittemeijer EJ (1988) *Metall Mater Trans A* 19:2433
- Cabibbo M, Evangelista E, Vedani M (2005) *Metall Mater Trans A* 35:1353
- Lee S, Utsunomiya A, Akamatsu H, Neishi K, Furukawa M, Horita Z, Langdon TG (2002) *Acta Mater* 50:553
- Marquis EA, Seidman DN (2001) *Acta Mater* 49:1909
- Davydov VG, Rostova TD, Zakharov VV, Yu A, Filatov VI, Yelagin (2000) *Mater Sci Eng A* 280:30
- Tolley A, Dahmen V, Radmilovic U (2005) *Scripta Mater* 52:621
- Iwamura S, Miura Y (2004) *Acta Mater* 52:591
- Sutton AP, Balluffi RW (1996) *Interfaces in crystalline materials*, Oxford University Press, Oxford
- Asta M, Foiles SM, Quong AA (1998) *Phys Rev B* 57:1265
- Vedani M, Bassani P, Cabibbo M, Latini V, Evangelista E (2003) *Metall Sci Technol* 21:3
- Dougherty LM, Robertson IM, Vetrano JS (2005) *Acta Mater* 51:4367